Electrical property mapping using MRI: analytical methods and implementations

Leijsen, R.L.

1

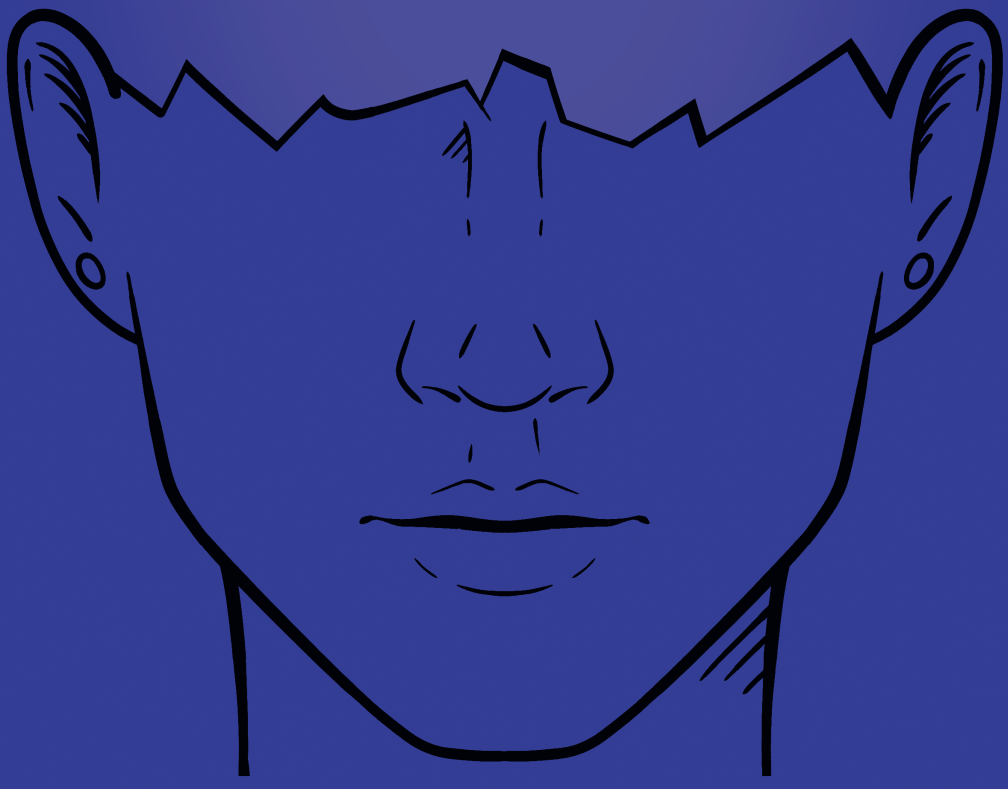

General Introduction

Een vader kan een vader zijn en moeder tegelijk
Da's een mooie theorie maar 't is een ramp in de praktijk

Kinderen voor kinderen - Moeders wil is wet, 1987

1

1.1. ELECTRICAL PROPERTIES

CONDUCTIVITY and permittivity are electrical quantities that describe the interaction of objects and electromagnetic fields. Conductivity (σ [S/m]) is a measure of how easily an electric charge (an intrinsic physical property of matter) can pass through a material. Permittivity (ε [F/m]) is a measure of the electric polarizability (the relative tendency of a charge distribution to be distorted from its normal shape by an external electric field) of a material. A material with a high conductivity allows for more current (flow of charged particles) to pass through and a material with a high permittivity polarizes more in response to an applied electric field than a material with a low conductivity and permittivity, respectively.

1.2. CLINICAL RELEVANCE

Tissue electrical properties (EPs) depend on the tissue structure and composition. The conductivity varies largely as a function of fluid volumes and ionic concentrations, while the permittivity is largely influenced by the cellular membrane extent [1]. The EPs of tissue have the potential to be used as biomarkers in many clinical applications. Cancer causes local changes of EPs relative to healthy tissues. The EPs of benign tissue compared to tumors is significantly different and have been reported to offer advantages in separating them from each other [2–4]. Similarly, the conductivity in cerebral ischemia is significantly decreased [5, 6]. Conductivity measurements can therefore be helpful for better characterization of brain tumors [7, 8], but have also shown promising results for pelvic tumors [9], breast cancer [10] and ischemic stroke [11, 12]. Knowledge of the EPs additionally allows for the calculation of the electromagnetic (EM) fields inside tissue. This makes them interesting for a wide range of clinical applications, such as electroencephalography (EEG) and electrocardiography (ECG) measurements to accurately localize internal electrical activities, deep brain stimulation to mitigate Parkinson's disease symptoms, radiofrequency (RF) ablation to remove arrhythmic genesis foci and RF hyperthermia for cancer treatment [13]. Additionally, they are critical to accurately determine the specific absorption rate (tissue heating) induced by EM waves [1].

1.3. ELECTRICAL PROPERTY MAPPING

Several EP mapping approaches are explored to map the electrical properties of tissue *in vivo*. Electrical impedance tomography (EIT), for example, uses electrode mounting to detect currents injected into the sample. This method is cost-effective and yields high temporal resolution, but poor spatial resolution due to the ill-posed nature of the inverse problem [13–15]. Magnetic induced tomography (MIT) detects perturbed magnetic field outside the object by using the interaction of an oscillating magnetic field with the EPs. However, it suffers from the same issues as EIT. Magnetic resonance electrical impedance tomography (MR-EIT) [16] utilizes MRI to detect the magnetic field induced by the probing current. This provides higher spatial resolution, but has a poor signal-to-noise ratio due to limitations on the amount of current injection [13, 17, 18]. Hall effect imaging (HEI) induces currents through surface electrodes and detects the emitted acoustic wave to reconstruct EPs [19]. This also has the potential to reach

high resolution images, but all of the current injection based methods may suffer from shielding artifacts of non-conducting tissue. Magneto-acoustic tomography with magnetic induction (MAT-MI) [20] circumvents this shielding problem by inducing acoustic signals with time varying magnetic fields which are detected with ultrasound measurements. However, methods that involve acoustic measurements are often limited to the surface of the object.

1.3.1. ELECTRICAL PROPERTIES TOMOGRAPHY

Electrical properties tomography (EPT) non-invasively images the conductivity and permittivity maps (simultaneously) *in vivo* from the radiofrequency field signals obtained with MRI. The method does not require electrode mounting, does not induce additional external energy other than the inherent RF fields and the RF fields can easily penetrate into most biological tissue. It typically uses a standard MRI system with regular RF coils. This concept was first introduced in 1991 by Haacke et al. [21] and first demonstrated in 2003 by Wen [22]. The topic, however, only recently gained considerable interest by various research groups [1, 13, 18, 23, 24].

1.4. RADIOFREQUENCY FIELD

In EPT there is one EM field of particular interest: the time-varying radiofrequency field $\boldsymbol{B}_1 = B_x\mathbf{i}_x + B_y\mathbf{i}_y$ that is perpendicular to the static main magnetic field $\boldsymbol{B}_0 = B_0(\boldsymbol{r})\mathbf{i}_z$ directed along the longitudinal z-direction. The radiofrequency field within the body contains information about the EPs of tissue, and phasors are typically used to describe its behavior. For a given time-domain RF field $\boldsymbol{B}_1(\boldsymbol{r},t)$ operating at a frequency $\omega > 0$ a phasor can be introduced via the representation

$$\boldsymbol{B}_1(\boldsymbol{r},t) = \mathrm{Re}\left[\hat{\boldsymbol{B}}_1\left(\boldsymbol{r},\mathrm{j}\omega\right)\exp\left(\mathrm{j}\omega t\right)\right]. \tag{1.1}$$

This $\boldsymbol{B}_1$ field can be written as the sum of two opposite rotating circularly polarized fields, $\boldsymbol{B}_1^+$ and $\boldsymbol{B}_1^-$, whose phasors are given by

$$\hat{\boldsymbol{B}}_1^+(\boldsymbol{r},\mathrm{j}\omega) = \hat{B}_1^+(\boldsymbol{r},\mathrm{j}\omega)(\mathbf{i}_x - \mathrm{j}\mathbf{i}_y) \quad \text{and} \quad \hat{\boldsymbol{B}}_1^-(\boldsymbol{r},\mathrm{j}\omega) = \left[\hat{B}_1^-(\boldsymbol{r},\mathrm{j}\omega)\right]^*(\mathbf{i}_x + \mathrm{j}\mathbf{i}_y), \tag{1.2}$$

where we have introduced the $\hat{B}_1^+$ and $\hat{B}_1^-$ fields defined as

$$\hat{B}_1^+(\boldsymbol{r},\mathrm{j}\omega) = \frac{\hat{B}_x(\boldsymbol{r},\mathrm{j}\omega) + \mathrm{j}\hat{B}_y(\boldsymbol{r},\mathrm{j}\omega)}{2} \quad \text{and} \quad \hat{B}_1^-(\boldsymbol{r},\mathrm{j}\omega) = \left[\frac{\hat{B}_x(\boldsymbol{r},\mathrm{j}\omega) - \mathrm{j}\hat{B}_y(\boldsymbol{r},\mathrm{j}\omega)}{2}\right]^*, \tag{1.3}$$

respectively. The direction of rotation of the polarized fields depends upon the direction of the static $\boldsymbol{B}_0$ field. If the reference frame is such that the static $\boldsymbol{B}_0$-field is in the negative z-direction ($\boldsymbol{B}_0 = -B_0(\boldsymbol{r})\mathbf{i}_z$ with $B_0(\boldsymbol{r}) > 0$), then the $\boldsymbol{B}_1^+$ and $\boldsymbol{B}_1^-$-fields rotate in a left- and right-handed manner about the $\boldsymbol{B}_0$ field, respectively.

In MRI the magnetization rotates in a left-handed manner about the $\boldsymbol{B}_0$-field. Radiofrequency fields that operate at the Larmor frequency and that rotate in the same manner about the $\boldsymbol{B}_0$ field as the magnetization are able to significantly influence the orientation of the magnetization, which ultimately leads to measurable MR signals.

The circularly polarized field is the one that is recognized as a more optimal polarization that provides high signal-to-noise ratio in an efficient way. In MRI literature, the left-handed circularly polarized RF field is always described in terms of a scalar $\hat{B}_1^+$-field, and since this enables the manipulation of magnetization it is called the transmit field. Similarly, received signals can be expressed in terms of the right-handed circularly polarized field, which is then completely described by the scalar $\hat{B}_1^-$-field and is therefore called the receive field.

1.5. MAGNETIC RESONANCE IMAGING

The transmit field can be written in polar form as $\hat{B}_1^+ = \left|\hat{B}_1^+\right| \exp(\mathrm{j}\hat{\varphi}^+)$, where $\left|\hat{B}_1^+\right|$ is the amplitude or magnitude of the transmit field and $\hat{\varphi}^+ \in (-\pi, \pi]$ its phase. Similarly, the receive field can be written in polar form as $\hat{B}_1^- = \left|\hat{B}_1^-\right| \exp\left(\mathrm{j}\hat{\varphi}^-\right)$, with $\left|\hat{B}_1^-\right|$ its amplitude and $\hat{\varphi}^- \in (-\pi, \pi]$ its phase. Spatial information is encoded into the signal using magnetic field gradients, applied after the $\hat{B}_1^+$ field has tipped the magnetization into the transverse plane. Due to the interaction with the body the transmit field has a spatial dependence, denoted $\hat{B}_1^+(\boldsymbol{r})$. This polar decomposition can be used to express the acquired spatially dependent MR image as [13, 18, 23, 25]

$$I(\boldsymbol{r}) = \underbrace{\sin\left(\gamma\tau\left|\hat{B}_1^+(\boldsymbol{r})\right|\right)}_{\substack{\text{non-linear}\\ \text{behaviour}}} \overbrace{\exp\left[\mathrm{j}\hat{\varphi}^\pm(\boldsymbol{r})\right]}^{\substack{\text{phase}\\ \text{entanglement}}} \underbrace{\varrho_0(\boldsymbol{r})\left|\hat{B}_1^-(\boldsymbol{r})\right|}_{\substack{\text{proton density}\\ \text{weighting}}}, \tag{1.4}$$

with ϱ_0 the proton density, γ the gyromagnetic ratio, τ the RF pulse duration and where $\hat{\varphi}^\pm = \hat{\varphi}^+ - \hat{\varphi}^-$ is the transceive phase. In this simplified expression for the acquired MR image, system dependent factors and contrast terms that underlie an MR image, such as T_1 and T_2 relaxation, are ignored. Of the transmit and receive field terms, only the magnitude of the transmit field shows a non-linear impact on the MR image. This non-linear relation allows for the direct measurement of the transmit phase by combining images from different scans such that confounding factors cancel. The magnitude of the transmit field can for example be acquired with the double-angle method (DAM) [26], actual flip angle imaging (AFI) [27, 28], dual refocusing echo acquisition mode (DREAM) [29, 30], or the Bloch-Siegert shift (BSS) [31, 32]. However, the acquired phase is always the superposition of the phases of $\hat{B}_1^+$ and $\hat{B}_1^{-;*}$, where $\hat{B}_1^{-;*}$ is the complex conjugate of $\hat{B}_1^-$, and can not be disentangled from measurements making it difficult to determine exactly. It has been observed that at 1.5 T and 3 T the transmit phase closely resembles the phase of $\hat{B}_1^{-;*}$, and in those cases the transmit phase is therefore typically estimated as half the transceive phase; this is termed the transceive phase assumption [22, 33]. The transceive phase can for example be acquired with spin echo (SE) sequences [34] or via steady-state free precession (SSFP) sequences [35, 36]. Similarly, the (magnitude of the) receive field is weighted by the proton density, which is also difficult to disentangle. If the proton density is not negligible, the proton density or magnitude of the receive field can be extracted from their product term based on symmetry patterns of the transmit and receive fields in the case of a symmetrical object and imaging setup [37, 38]. Additionally, the proton density could be removed via

suitable modeling based on image segmentation [37]. Note, however, that knowledge of the transmit phase, receive phase or receive magnitude individually is not always necessary in EPT, but could also potentially be determined *through* EPT.

1.6. EPT CATEGORISATION

Even though the EPT research field is relatively young, the list of EPT techniques is quite extensive. In order to cast some light into the darkness, the reconstruction approaches can, for example, be categorized in the *type of data input* they use. Some methods require knowledge of the transmit (e.g. Helmholtz-based EPT [21]) and/or receive field (e.g. single-acquisition EPT [39]), or only its magnitude or phase (e.g. simplified Helmholtz-based EPT [40]), while others use the MR image as input (e.g. image-based EPT [41]). Similarly, the methods can be categorized on the *type of model* they employ. There are methods that are based on a physical model (e.g. first-order induced current EPT [42] and Cauchy-based EPT [43]), while others are based on a set of example data (e.g. dictionary-based EPT [44] and deep learning EPT [45]). Most often the techniques are categorized in the *way they utilize* input data. For example, whether the method applied differentials (e.g. convection-reaction EPT [46]) or integrals (e.g. variational Born iterative method EPT [47]), whether it acts locally (e.g. local Maxwell tomography [48]) or globally (e.g. global Maxwell tomography [49]), or whether it acts directly (e.g. gradient-based EPT [50]) or 'indirectly' (e.g. contrast source inversion EPT [51]) on the data. Each category is accompanied by its own benefits and weaknesses.

1.7. THESIS AIM AND OUTLINE

The aim of this thesis is to develop noise robust EPT reconstruction methods that are free from tissue transition artifacts to support clinical applications for complex tissue structures such as the brain. In particular the contrast-source inversion approach is pursued. This thesis will focus on the reconstruction of the EPs from the transmit field (the so called $\hat{B}_1^+$-field) of RF coils most frequently available in MRI.

Chapter 2 of this thesis starts with the introduction of a novel reconstruction method called three-dimensional contrast source inversion-electrical properties tomography (3D CSI-EPT). The method is based on integral representations of the electromagnetic field and allows EP reconstructions of small structures as well as tissue boundaries with compelling accuracy and with exceptional noise robustness. Moreover, the three-dimensional extension is not restricted to E-polarized field structures and can be applied to realistic 3D scenarios.

Chapter 3 reviews the basics of first-order induced current EPT (foIC-EPT) and 2D and 3D CSI-EPT, and presents several comparisons between the reconstructions obtained with each method. It extensively discusses the limitations of a two-dimensional approach and shows that E-polarized field assumptions in foIC-EPT and 2D CSI-EPT are only allowed if longitudinal invariance or smoothness of certain field components can be guaranteed, while this is not required for 3D CSI-EPT. Furthermore, several practical implementation issues are addressed as well.

Chapter 4 investigates the benefits achievable by using a combination of 3D CSI-EPT with a machine learning EPT approach. Deep learning EPT requires a large train-

ing dataset to allow for better generalization, while CSI-EPT depends on the map provided as initialization. A hybrid method consisting of an initial deep learning EPT reconstruction followed by a 3D CSI-EPT reconstruction facilitates a better generalization, since CSI-EPT introduces data consistency, while a DL-EPT initialization would be more beneficial than a conventional Helmholtz-based initialization for CSI-EPT.

Chapter 5 compares different 3D CSI-EPT strategies, among one contains total-variation regularization and investigates the effects of a large number of simulated error-sources such as noise, incident fields, initialization and domain truncation. These insights are required to understand the origin and effect of errors, and to help the step towards clinical application. An overview of the iterative structure of CSI-EPT is provided as well

Chapter 6 introduces another novel reconstruction method, called transverse EPT (T-EPT). In contrast to conventional Helmholtz-based EPT, this approach does not require spatial homogeneity of tissue structures and involves only first order derivatives, resulting in better boundary conditions and improved noise robustness. Similar to 2D CSI-EPT, the EPs are updated in an iterative fashion and the E-polarized field structure typically present in the midplane of a birdcage radiofrequency coil is exploited to allow for fast reconstructions. However, T-EPT has the additional benefit that it does not require knowledge of the incident fields.

Chapter 7 reviews a large number of available analytical EPT approaches in a methodological way and harmonizes them in a single type of formulation. This gives insight into what their data requirements are and how they act on the data.

Chapter 8 finally presents a summary and discusses the previous chapters.

REFERENCES

[1] X. Zhang, J. Liu, and B. He, *Magnetic-resonance-based electrical properties tomography: a review,* IEEE Rev. Biomed. Eng. **7**, 87 (2014).

[2] A. J. Surowiec, S. S. Stuchly, J. R. Barr, and A. Swarup, *Dielectric properties of breast carcinoma and the surrounding tissues,* IEEE. Trans. Biomed. Eng. **35**, 257 (1988).

[3] Y. Lu, B. Li, J. Xu, and J. Yu, *Dielectric properties of human glioma and surrounding tissue,* Int. J. Hyperthermia **8**, 755 (1992).

[4] I. Hancu, J. C. Roberts, S. Bulumulla, and S.-K. Lee, *On conductivity, permittivity, apparent diffusion coefficient, and their usefulness as cancer markers at MRI frequencies,* Magn. Reson. Med. **73**, 2025 (2015).

[5] D. S. Holder, *Detection of cerebral ischaemia in the anaesthetised rat by impedance measurement with scalp electrodes: Implications for non-invasive imaging of stroke by electrical impedance tomography,* Clin. Phys. Physiol. Meas. **13**, 63 (1992).

[6] M. A. Fallert, M. S. Mirotznik, S. W. Downing, *et al.*, *Myocardial electrical impedance mapping of ischemic sheep hearts and healing aneurysms,* Circulation **87**, 199 (1993).

[7] K. K. Tha, C. Stehning, Y. Suzuki, *et al.*, *Noninvasive evaluation of electrical conductivity of the normal brain and brain tumors,* in *Proc Int Soc Magn Reson Med*, Vol. 22 (2014) p. 1885.

[8] K. K. Tha, U. Katscher, S. Yamaguchi, *et al.*, *Noninvasive electrical conductivity measurement by MRI: a test of its validity and the electrical conductivity characteristics of glioma,* Eur. Radiol. **28**, 348 (2018).

[9] E. Balidemaj, A. L. van Lier, H. Crezee, A. J. Nederveen, L. J. Stalpers, and C. A. van den Berg, *Feasibility of electric property tomography of pelvic tumors at 3 T,* Magn. Reson. Med. **73**, 1505 (2015).

[10] J. Shin, M. J. Kim, J. Lee, *et al.*, *Initial study on in vivo conductivity mapping of breast cancer using MRI,* J. Magn. Reson. Imaging **42**, 371 (2015).

[11] A. van Lier, A. Kolk, M. Brundel, *et al.*, *Electrical conductivity in ischemic stroke at 7.0 tesla: a case study,* in *Proceedings of the 20th Scientific Meeting of the International Society of Magnetic Resonance in Medicine (ISMRM'12)*, Vol. 3484 (2012).

[12] N. Gurler, O. F. Oran, H. D. Keklikoglu, and Y. Z. Ider, *Application of generalized phase based electrical conductivity imaging in the subacute stage of hemorrhagic and ischemic strokes,* in *Proc. 24th Annu. Meeting ISMRM* (2016) p. 2994.

[13] J. Liu, Y. Wang, U. Katscher, and B. He, *Electrical properties tomography based on B_1 maps in MRI: Principles, applications, and challenges,* IEEE. Trans. Biomed. Eng. **64**, 2515 (2017).

[14] B. H. Brown, *Electrical impedance tomography (EIT): a review,* J. Med. Eng. Technol. **27**, 97 (2003).

[15] X. Zhang, P.-F. van de Moortele, S. Schmitter, and B. He, *Complex B_1 mapping and electrical properties imaging of the human brain using a 16-channel transceiver coil at 7 T,* Magn. Reson. Med. **69**, 1285 (2013).

[16] E. J. Woo, S. Y. Lee, and C. W. Mun, *Impedance tomography using internal current density distribution measured by nuclear magnetic resonance,* in *Mathematical Methods in Medical Imaging III*, Vol. 2299 (International Society for Optics and Photonics, 1994) pp. 377–385.

[17] E. J. Woo and J. K. Seo, *Magnetic resonance electrical impedance tomography (MREIT) for high-resolution conductivity imaging,* Physiol. Meas. **29**, R1 (2008).

[18] U. Katscher, D.-H. Kim, and J. K. Seo, *Recent progress and future challenges in MR electric properties tomography,* Comput. Math. Method. M. **2013**, 1 (2013).

[19] H. Wen, J. Shah, and R. S. Balaban, *Hall effect imaging,* IEEE. Trans. Biomed. Eng. **45**, 119 (1998).

[20] Y. Xu and B. He, *Magnetoacoustic tomography with magnetic induction (MAT-MI),* Phys. Med. Biol. **50**, 5175 (2005).

[21] E. M. Haacke, L. S. Petropoulos, E. W. Nilges, and D. H. Wu, *Extraction of conductivity and permittivity using magnetic resonance imaging,* Phys. Med. Biol. **36**, 723 (1991).

[22] H. Wen, *Noninvasive quantitative mapping of conductivity and dielectric distributions using RF wave propagation effects in high-field MRI,* in *Proc. SPIE*, Vol. 5030 (San Diego, CA, USA, 2003) pp. 471–477.

[23] U. Katscher and C. A. T. van den Berg, *Electric properties tomography: Biochemical, physical and technical background, evaluation and clinical applications,* NMR Biomed. **30**, e3729 (2017).

[24] R. Leijsen, W. Brink, C. van den Berg, A. Webb, and R. Remis, *Electrical properties tomography: A methodological review,* Diagnostics **11**, 176 (2021).

[25] D. I. Hoult, *The principle of reciprocity in signal strength calculations–a mathematical guide,* Concepts Magn. Res. **12**, 173 (2000).

[26] E. Insko and L. Bolinger, *Mapping of the radiofrequency field,* J. Magn. Reson. **103**, 82 (1993).

[27] V. L. Yarnykh, *Optimal radiofrequency and gradient spoiling for improved accuracy of T_1 and B_1 measurements using fast steady-state techniques,* Magn. Reson. Med. **63**, 1610 (2010).

[28] G. R. Morrell and M. C. Schabel, *An analysis of the accuracy of magnetic resonance flip angle measurement methods,* Phys. Med. Biol. **55**, 6157 (2010).

[29] K. Nehrke and P. Börnert, *DREAM–a novel approach for robust, ultrafast, multislice B_1 mapping,* Magn. Reson. Med. **68**, 1517 (2012).

[30] K. Nehrke, M. J. Versluis, A. Webb, and P. Börnert, *Volumetric B_1^+ mapping of the brain at 7 T using DREAM,* Magn. Reson. Med. **71**, 246 (2014).

[31] L. I. Sacolick, F. Wiesinger, I. Hancu, and M. W. Vogel, *B_1 mapping by bloch-siegert shift,* Magn. Reson. Med. **63**, 1315 (2010).

[32] E. A. Turk, Y. Z. Ider, A. S. Ergun, and E. Atalar, *Approximate fourier domain expression for bloch–siegert shift,* Magn. Reson. Med. **73**, 117 (2015).

[33] A. L. H. M. W. van Lier, A. Raaijmakers, T. Voigt, *et al.*, *Electrical properties tomography in the human brain at 1.5, 3, and 7 T: a comparison study,* Magn. Reson. Med. **71**, 354 (2014).

[34] A. L. van Lier, D. O. Brunner, K. P. Pruessmann, *et al.*, *B_1^+ phase mapping at 7 T and its application for in vivo electrical conductivity mapping,* Magn. Reson. Med. **67**, 552 (2012).

[35] S. Ozdemir and Y. Z. Ider, *bSSFP phase correction and its use in magnetic resonance electrical properties tomography,* Magn. Reson. Med. **81**, 934 (2019).

[36] S. Gavazzi, Y. Shcherbakova, L. W. Bartels, *et al.*, *Transceive phase mapping using the planet method and its application for conductivity mapping in the brain,* Magn. Reson. Med. **83**, 590 (2020).

[37] U. Katscher, C. Findeklee, and T. Voigt, *B_1-based specific energy absorption rate determination for nonquadrature radiofrequency excitation,* Magn. Reson. Med. **68**, 1911 (2012).

[38] X. Zhang, S. Schmitter, P.-F. van de Moortele, J. Liu, and B. He, *From complex B_1 mapping to local SAR estimation for human brain MR imaging using multichannel transceiver coil at 7 T,* IEEE Trans. Med. Imaging **32**, 1058 (2013).

[39] J. P. Marques, D. K. Sodickson, O. Ipek, C. M. Collins, and R. Gruetter, *Single acquisition electrical property mapping based on relative coil sensitivities: a proof-of-concept demonstration,* Magn. Reson. Med. **74**, 185 (2015).

[40] T. Voigt, U. Katscher, and O. Doessel, *Quantitative conductivity and permittivity imaging of the human brain using electric properties tomography,* Magn. Reson. Med. **66**, 456 (2011).

[41] P. Soullié, A. Missoffe, K. Ambarki, J. Felblinger, and F. Odille, *MR electrical properties imaging using a generalized image-based method,* Magn. Reson. Med. **85**, 762 (2021).

[42] P. S. Fuchs, S. Mandija, P. R. Stijnman, W. M. Brink, C. A. van den Berg, and R. F. Remis, *First-order induced current density imaging and electrical properties tomography in MRI,* IEEE Trans. Comput. Imaging **4**, 624 (2018).

[43] M. Fushimi and T. Nara, *Boundary value-free magnetic resonance electrical properties tomography based on the generalized cauchy formula with the complex-derivative boundary condition,* Prog. Electromagn. Res. M **96**, 1 (2020).

[44] N. Hampe, M. Herrmann, T. Amthor, C. Findeklee, M. Doneva, and U. Katscher, *Dictionary-based electric properties tomography,* Magn. Reson. Med. **81**, 342 (2019).

[45] S. Mandija, E. F. Meliadò, N. R. Huttinga, P. R. Luijten, and C. A. van den Berg, *Opening a new window on MR-based electrical properties tomography with deep learning,* Sci. Rep. **9**, 1 (2019).

[46] F. S. Hafalir, O. F. Oran, N. Gurler, and Y. Z. Ider, *Convection-reaction equation based magnetic resonance electrical properties tomography (cr-MREPT),* IEEE Trans. Med. Imaging **33**, 777 (2014).

[47] R. Hong, S. Li, J. Zhang, *et al.*, *3-D MRI-based electrical properties tomography using the volume integral equation method,* IEEE Trans. Microw. Theory Tech. **65**, 4802 (2017).

[48] D. K. Sodickson, L. Alon, C. M. Deniz, *et al.*, *Generalized local Maxwell tomography for mapping of electrical property gradients and tensors,* in *Proc. Int. Soc. Mag. Reson. Med.* (2013) p. 4175.

[49] J. E. Serrallés, I. I. Giannakopoulos, B. Zhang, *et al.*, *Noninvasive estimation of electrical properties from magnetic resonance measurements via global Maxwell tomography and match regularization,* IEEE. Trans. Biomed. Eng. **67**, 3 (2019).

[50] J. Liu, X. Zhang, S. Schmitter, P.-F. van de Moortele, and B. He, *Gradient-based electrical properties tomography (gEPT): A robust method for mapping electrical properties of biological tissues in vivo using magnetic resonance imaging,* Magn. Reson. Med. **74**, 634 (2015).

[51] R. L. Leijsen, W. M. Brink, C. A. van den Berg, A. G. Webb, and R. F. Remis, *3-D contrast source inversion-electrical properties tomography,* IEEE Trans. Med. Imaging **37**, 2080 (2018).